Interaction of regular and extreme waves with submerged cylinders

R. W. Yeung, S.-W. Liao and D. Roddier
Mechanical Engineering / Ocean Engineering
University of California at Berkeley, Berkeley, California 94720-1740, USA

1 Introduction

Wave forces on a cylinder have been a topic of great interest, since correct estimation of forces is important for the design of a structure that can meet safety standards. In the past, the attention had been on oscillatory flows past a cylinder, which is analogous to wave flows past a cross section of a vertical cylinder. On the other hand, the flow around a horizontal cylinder, with its axis parallel to the wave crests, is different from that of a vertical cylinder.

Experiments by Koterayama and Tasiro (1978) showed that there are discrepancies in the hydrodynamic coefficients between oscillatory and orbital flows. Later, Chaplin (1984a,b) applied boundary-layer analysis to show that the effects of oscillatory boundary layer around a circular cylinder in orbital flows may be similar to those by a potential vortex around the cylinder. The vortex, whose strength may be independent on the fluid viscosity, caused the wave forces on the cylinder to be smaller than thosed predicted by the inviscid solution such as Ogilivie (1963). Flow observation by Otsuka, *et al.* (1990) confirmed the induced circulation around a circular cylinder.

A few cases of study of orbital flows past a cylinder exist, e.g., Tiemroth (1986), Stansby and Smith (1991), Landrini, *et al.* (1997). This paper presents a numerical wave tank that can simulate surface waves passing over submerged cylinders with the effects of separation included. The wave-generation algorithm for a wavemaker (Liao & Roddier, 1998) is combined with the Free-Surface Random-Vortex Method "FSRVM" (Yeung & Vaidhyanathan, 1994) to study the interaction of both regular and extreme waves with submerged cylinders. Viscous effects, which include the force reduction and induced circulation, are examined for a circular cylinder. For extreme waves, a case is studied for a square cylinder with rounded corners.

2 Generation of extreme waves

Generation of deep-water extreme waves involves superposing waves of different frequencies in a way such that the crests focus at a given location and time. Its generation in laboratory relies on properly specifying the wavemaker motion. When a working spectrum exists (e.g., Dommermuth, *et al.*, 1988), we have developed a procedure that can be used to translate the wave group so that extreme waves will occur at any desired locations in the wave tank.

Figure 1 shows a wave tank featuring a paddle wavemaker. Let the wavemaker motion be consisted of a finite Fourier series with M components, surrounding a central frequency ω_c, and its motion at $y = 0$ is:

$$S(y{=}0,t) = \sum_{i=1}^{M} S_i \sin(\omega_i t - \varphi_i), \tag{1}$$

where S_i and φ_i are the amplitude and phase angle for the ith frequency component ω_i. Based on linear theory (Wehausen and Laitone, 1960), the corresponding "far-field" solution for the potential is:

$$\phi = \sum_{i=1}^{M} \frac{A_i\, g\, \cosh k_i(y+h)}{\omega_i\, \cosh k_i h} \sin(k_i x - \omega_i t + \varphi_i + k_i L_t) \tag{2}$$

for $(x + L_t) \gg h$, where the wave amplitude to stroke amplitude ratio is:

$$\frac{A_i}{S_i} = 4\left(\frac{\sinh k_i h}{k_i h}\right) \frac{k_i h \sinh k_i h - \cosh k_i h + 1}{\sinh 2k_i h + 2k_i h}. \tag{3}$$

Let x^* and t^* be the location and time when the extreme waves occur for an original wavemaker input of $(S_i, \omega_i, \varphi_i)$. According to linear theory, the free surface profile is

$$\eta(x^*, t^*) = \sum_{i=1}^{M} A_i \cos(k_i x^* - \omega_i t^* + \varphi_i + k_i L_t). \tag{4}$$

In order to translate this "target profile", it is desirable to find new $\bar{\varphi}_i$ without altering S_i and ω_i. For a new location of the target profile at

$$\bar{x}^* = x^* + \chi, \quad \text{and} \quad \bar{t}^* = t^* + \tau, \tag{5}$$

the displacement in time τ is related to the displacement in space χ by

$$\tau = \frac{\chi}{c_g}, \quad c_g = \frac{1}{2}\frac{\omega_c}{k_c}, \tag{6}$$

where k_c and c_g are the wavenumber and group velocity corresponding to ω_c of the wave group. The new surface profile at $(\bar{x}^*, \bar{t}^*)$ is

$$\eta(\bar{x}^*, \bar{t}^*) = \sum_{i=1}^{M} A_i \cos(k_i \bar{x}^* - \omega_i \bar{t}^* + \bar{\varphi}_i + k_i L_t) = \sum_{i=1}^{M} A_i \cos$$

$$\{k_i x^* - \omega_i t^* + \varphi_i + k_i L_t + [\bar{\varphi}_i - \varphi_i + k_i \chi - \omega_i \tau]\}, \tag{7}$$

where $\bar{\varphi}_i$ is to be determined. If this profile is to be identical to $\eta(x^*, t^*)$, then the bracket quantity in Eqn. (7) vanishes:

$$\bar{\varphi}_i = \varphi_i - k_i \chi + \omega_i \tau. \tag{8}$$

Equation (8) therefore specifies the new component phase angles $\bar{\varphi}_i$ completely.

Another alternative is to apply Froude scaling (Liao and Roddier, 1998), by which all ω_is are scaled by the same factor, resulting extreme waves with a different ω_c. This, however, may change S_i undesirably.

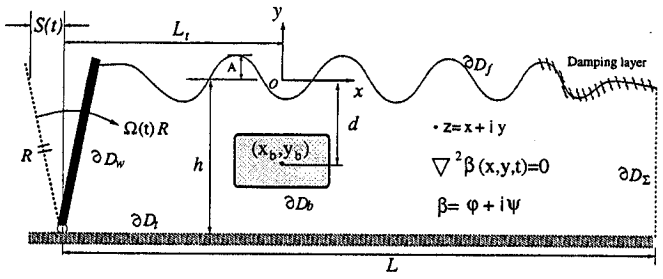

Figure 1: Definitions and the computational domain D.

3 Principles of the FSRVM

The FSRVM of Yeung and Vaidhyanathan (1994) consists of decomposing the flow field into vortical and irrotational parts. The vortical part of the flow is solved using the RVM (Chorin, 1973) and the irrotational part of the flow is solved by a Complex-Variable Boundary-Element Method (Grosnbaugh & Yeung, 1989). Validation of the FSRVM can be found in Yeung *et al.* (1998), Yeung & Cermelli (1998). Its grid-free property makes it very attractive. The governing equations for two-dimensional incompressible viscous fluid using a vorticity and stream-function formulation are:

$$\frac{D\xi}{Dt} = \nu\nabla^2\xi, \tag{9}$$

$$\nabla^2\psi = -\xi, \tag{10}$$

where $\xi\mathbf{k}=\nabla\times\mathbf{u}$ and D/Dt is the material derivative. The velocity vector $\mathbf{u}$ is given in terms of ψ by $(\psi_y, -\psi_x)$. To model the vorticity field, it is assumed to be a collection of "blobs" with finite core size:

$$\xi(\mathbf{x},t) = \sum_{i=1}^{N(t)} \Gamma_i f(\mathbf{x}-\mathbf{x}_i(t)), \tag{11}$$

where ξ is the vorticity at a field point $\mathbf{x}$, and $\mathbf{x}_i$ is the location of a blob with strength of circulation Γ_i. f is a function representing the vorticity distribution within a finite-size core of the blob.

The vorticity transport equation (9) is solved by a fractional step method: consisting of a convection step and a diffusion step at successive half time-steps. At the convection step, blobs are convected according to the fluid velocity. At the diffusion step, every blob is given an independent random walk with standard deviation $\sqrt{2\nu\Delta t}$ for each time step.

For convection, $\mathbf{u}$ is obtained by solving for the stream function. ψ is written as a sum of a vortical part and a homogeneous part,

$$\psi = \psi_v + \psi_h, \text{ where } \nabla^2\psi_v = -\xi, \ \nabla^2\psi_h = 0. \tag{12}$$

Since the vorticity field is assumed to be represented by Eqn. (11), ψ_v is known. It follows that that only ψ_h needs to be determined. This is accomplished by solving for ψ_h using a complex potential formulation $\beta_h = \phi_h + i\psi_h$ similar to Grosenbaugh & Yeung (1989). With reference to Fig. 1, the "no-leak" condition is used on ∂D_w, ∂D_t, and ∂D_b. On the free surface ∂D_f, an inviscid boundary condition can be used as the shear-layer on the free surface is expected to have relatively weak effects on the solution. Finally, on the open boundary ∂D_Σ, a non-disturbance condition can be applied for sufficiently large distance from the body. These boundary conditions are used to set up a Cauchy's integral equation for β_h, where either ϕ_h or ψ_h is specified on ∂D:

$$\pi i\beta_h(z) - \oint_{\partial D} \frac{\beta_h(\zeta)}{\zeta - z} d\zeta = 0 \text{ for } z \in \partial D. \tag{13}$$

The no-slip boundary condition on the body surface is satisfied by generating surface vorticity to nullify the tangential velocity induced by ψ. A similar integral-equation can be set up for $\hat{\beta}_h$ in order to calculate the forces on the body based on Euler's integral.

4 Regular waves past a circular cylinder

Results of regular waves moving past a circular cylinder are presented in this section for $A = 4.9$ cm, $T = 1.6$ sec, $\lambda = 400$ cm, and $h = 300$ cm. The dimensions of the circular cylinder are: $B = 8$ cm for the diameter, and $d = 16$ cm for the submergence, chosen to be compatible with the experiments of Ikeda (1988). The distance between the wavemaker and the cylinder center is 2λ.

Based on the Morison equation, the wave forces are approximated by

$$F_x(t) = \rho C m_x \forall \dot{U} + \tfrac{1}{2}\rho C d_x B U|U|, \tag{14}$$

$$F_y(t) = \rho C m_y \forall \dot{V} + \tfrac{1}{2}\rho C d_y B V|V|, \tag{15}$$

where Cm and Cd are "best-fit" inertia and drag coefficients, $\forall$ is the section area; $(\dot{U}, \dot{V})$ and (U, V) are the fluid acceleration and velocity vectors at $(0, -h)$ when the body is not present, calculatable from Eqn. (2). The hydrodynamic coefficients Cm and Cd can be extracted from the force time history using Fourier analysis (Sarpkaya & Isaacson, 1981). It can be shown that

$$\frac{F^{inertia}}{F^{drag}} = \frac{2\pi}{KC}\frac{Cm}{Cd}, \ KC = \frac{U_a T}{B}, \tag{16}$$

where U_a is the amplitude of U. For low KC, the inertia term dominates and a reduction of Cm would result in smaller wave forces.

Chaplin (1984b) provided an empirical estimate of the inertia coefficient for orbital flow at low KC:

$$Cm = 2 - 0.21KC^2 \tag{17}$$

which is useful for comparison purposes. Cm attains a value of 2.0 for inviscid linear flow.

For $KC = 3$, the inertia and drag coefficients extracted from FSRVM, using a time window of $3.2T$, are shown in Fig. 2 as functions of time. The Cm values of the *inviscid* run is about 2 as predicted by the linear theory. However, Cm values of the viscous results are significantly reduced. Although Cm in Fig. 2 is different from what Eqn. (16) estimates, they agree with the experimental results in Arai (1995), $[Cm_x, Cm_y]$=[1.2,1]. Compared with the inertia coefficients, the drag coefficients are not as steady. Table 1 shows the comparison of experimental and FSRVM inertia coefficients for $KC = 1$ and 2. The agreement is also very good for these two cases.

Figure 3 shows the blobs and streamlines around the cylinder for $t/T = 10$ to 10.75, 1/4-period apart. The blobs appear to undergo a steady circular motion around the cylinder, and there is no tendency for the blobs to move towards the free surface. Note the resemblance between the streamlines in Fig. 3 and those of a rotating cylinder in uniform flow. This is consistent with the existence of a steady circulation as reported by Chaplin (1984a). Using a different model, Chaplin (1993) has obtained similar streamlines around the cylinder.

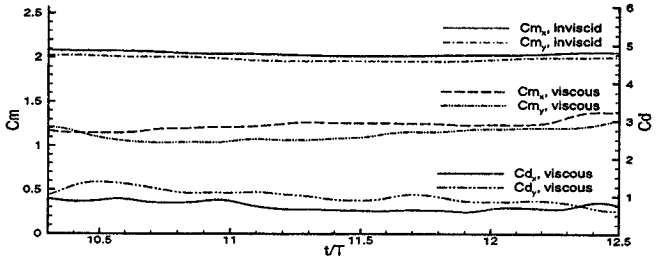

Figure 2: Comparison of inertia coefficients for inviscid and viscous cases, KC=3.

	Cm_x			Cm_y		
	Arai	Ikeda	FSRVM	Arai	Ikeda	FSRVM
KC=1	–	1.75	1.65	–	1.75	1.58
KC=2	1.18	1.2	1.32	1.2	1.22	1.18

Table 1: Experimental and numerical Cm.

5 Extreme waves past a cylinder

In this section, the wave-generation algorithm of §2 is applied to create an extreme wave propagating over a cylinder. The design location of a plunging breaker is 12.5 m from the wavemaker, where h = 150 cm. At the design location, a square cylinder, with B = 10 cm and corner radius of 2 cm, is placed at d = 35 cm.

The displacement $S(y{=}0,t)$ is shown in Fig. 4 with central period T = 1.75 sec for the wavemaker motion and wave group. Note the trend that the frequency of the motion is decreasing in time. Physically, this means that shorter waves are first generated and will be caught up by longer waves. This reinforcement of waves results in a high-amplitude crest at $t/T = 9$.

Figures 5 and 6 show the forces on the cylinder in the horizontal and vertical directions. These forces are normalized:

$$\tilde{F}_x(t) = \frac{F_x(t)}{\rho \forall \omega_c \sqrt{gh}}, \quad \tilde{F}_y(t) = \frac{F_y(t)}{\rho \forall \omega_c \sqrt{gh}}. \qquad (18)$$

For $\tilde{F}_x$, the effects of viscosity does not show up until $t/T > 8.3$. The magnitudes of $\tilde{F}_x$ are about the same until $t/T = 8.5$. For both runs, the maximum of $\tilde{F}_x$ occurs when the breaker is right on top of the cylinder, $t/T = 9.35$. However, $\tilde{F}_x$ of the inviscid run is 70% greater than that of the viscous run when $\tilde{F}_x$ is maximum. For $\tilde{F}_y$, these two records are very similar for $0 \le t/T \le 8$ except for $6.4 \le t/T \le 7.2$. When $t/T > 8$, there is a phase lag between these two records. The peak at $t/T = 9.1$ of the inviscid run occurs when the trough is passing over the cylinder, while the peak occurs at $t/T = 9.2$ for the viscous run. Next, $\tilde{F}_y$ of the inviscid run quickly turns negative, while $\tilde{F}_y$ of the viscous run is still positive when the simulation ends.

Figure 7 shows the evolution of the free surface and its interaction with the vortex blobs around the cylinder prior to wave plunging. The crest appears at $t/T = 9.15$. The front face of breaker continues to steepen, which becomes vertical at $t/T = 9.2$. Next, a jet is formed at the crest and becoming a plunging breaker at $t/T = 9.35$. As the free surface starts to rise ($t/T = 9$) till it overturns ($t/T = 9.35$), the blobs system appear to undergo a counter-clockwise motion around the cylinder. Although the waves consist 72 frequency components, the behavior of the blobs are similar to that shown in Fig. 3, where there is only one frequency component. This may explain why the forces of the viscous run are smaller than those of the inviscid run.

6 Conclusions

A numerical wave tank is presented to study both regular and extreme waves passing over submerged cylinders. A wave-generation algorithm is developed to produce extreme waves at specific locations and time in a wave tank. It is combined with the FSRVM so that the Navier Stokes equations are solved for the flows around the cylinders.

For regular waves past a circular cylinder, results of numerical simulations agree well with experimental data in terms of the Cm values. The calculated flow patterns around the cylinder also show the characteristics of an induced circulation. A case of extreme waves passing over a square cylinder is presented to study the effects of viscosity. Similar to the regular-wave case, it is observed that the forces are smaller than those predicted by inviscid theory. The blobs around the cylinder also have a behavior similar to that in the regular-wave case, namely, the blobs follow the fluid motion around the cylinder.

These initial results are encouraging for a successful numerical wave tank development, which can be used to study nonlinear wave-structure interaction of other geometry and scenarios.

References

Arai, S. (1995). *Proceedings, 5th Int'l Offshore and Polar Engrg. Conf.*, **3**, pp. 348–355.

Chaplin, J. R. (1984a). *J. Fluid Mech*, **140**, pp. 175–187.

Chaplin, J. R. (1984b). *J. Fluid Mech*, **147**, pp. 449–464.

Chaplin, J. R. (1993). *J. Fluid Mech*, **246**, pp. 397–418.

Chorin, A. J. (1973). *J. Fluid Mech.*, **57**, pp. 785–796.

Dommermuth, D. G., Yue, D. K. P., Lin, W. M., Rapp, R. J., Chan, E. S., and Melville, W. K. (1988). *J. Fluid Mech.*, **189**, pp. 423–442.

Grosenbaugh, M. A. and Yeung, R. W. (1989). *J. Fluid Mech.*, **209**, pp. 57–75.

Ikeda, Y., Otsuka, K., and Tanaka, N. (1988). *J. of the Society of Naval Arch. of Japan*, **163**, pp. 214–221.

Koterayama, W. and Tashiro, A. (1978). *J. of the Society of Naval Architects of Japan*, **143**, pp. 136–144.

Landrini, M., Ranucci, M., Casciola, C.M., and Graziani, G. (1997). *Proc. 12th Int. Workshop on Water Waves and Floating Bodies*, Marseille, France, pp. 147-150.

Liao, S.-W., and Roddier, D. (1998). OEG-98.1, Ocean Engineering Group, University of California, Berkeley.

Ogilvie, T. F. (1963). *J. Fluid Mech.*, **16** pp. 451–472.

Otsuka, K., Ikeda, Y., and Tanaka, N. (1990). *Proc., 9th OMAE Symp.*, **1**, Part A, pp. 129–138.

Sarpkaya, T. and Isaacson, M. (1981). *Mechanics of wave forces on offshore structures*, van Nostrand Reinhold Company.

Stansby, P. K. and Smith P. A. (1991). *J. Fluid Mech.*, **229**, pp. 159–171.

Tiemroth, E. C. (1986). *Proc. 16th ONR Symp. on Naval Hydrodyn.*, Berkeley, CA, pp. 490–513.

Wehausen, J. V. and Laitone, E. V. (1960). "Surface Waves", in *Handbuch der Physik*, **9**, Springer-Verlag.

Yeung, R. W. and Vaidhyanathan, M. (1994). *Proceedings, Int'l. Conference on Hydrodynamics*, pp 118-128, Wuxi, China.

Yeung, R. W. and Cermelli, C. A. (1998), Chapter 1, *Free Surface Flow with Viscosity*, Advances in Fluid Mechanics, vol. 16, ed. P. Tyvand, Computational Mechanics Publications, Southampton, England.

Yeung, R. W., Liao, S.-W., and Roddier, D. (1998). *Int. J. of Offshore & Polar Engrg.*, **8**, pp. 241–250.

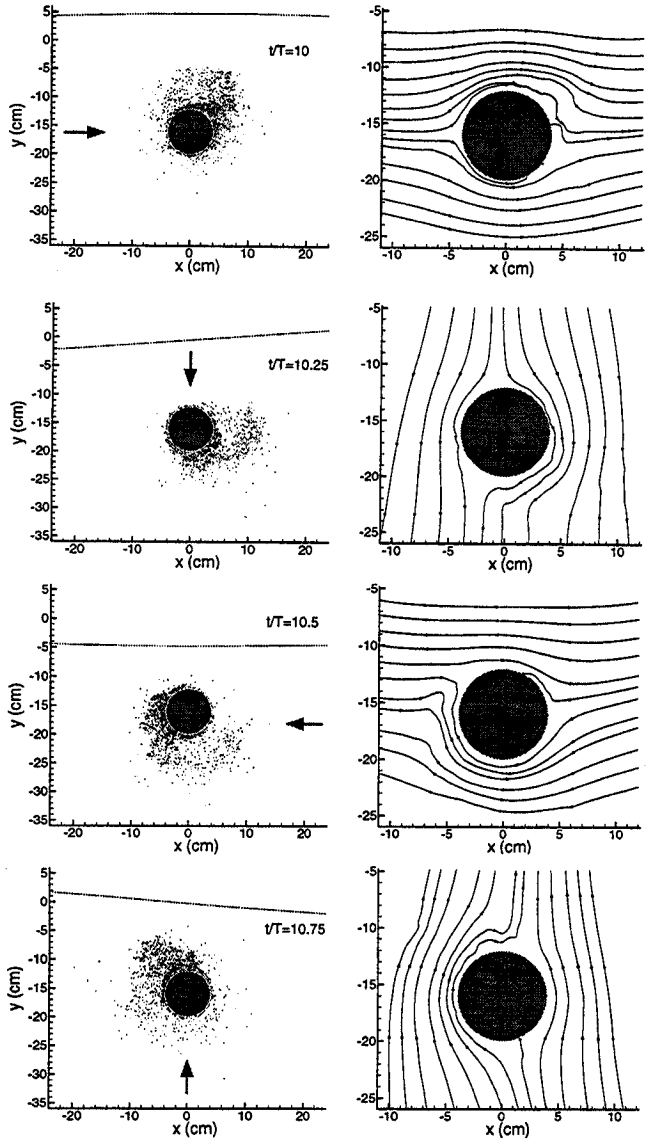

Figure 3: *Right*: Blobs around the circular cylinder under the waves. *Left*: Streamlines near the cylinder. From top to bottom, $t/T = 10$, 10.25, 10.5, 10.75, $KC = 3$.

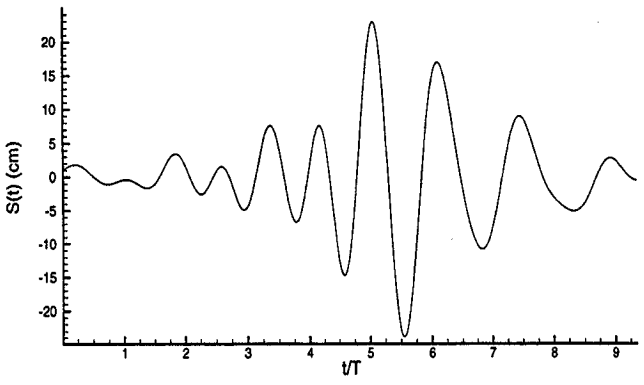

Figure 4: Time history of the wavemaker displacement at y=0.

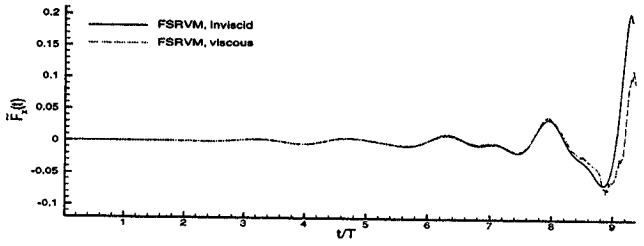

Figure 5: Comparison of forces in horizontal direction for inviscid and viscous results.

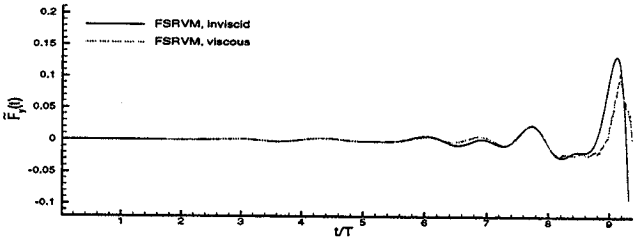

Figure 6: Comparison of forces in vertical direction for inviscid and viscous results.

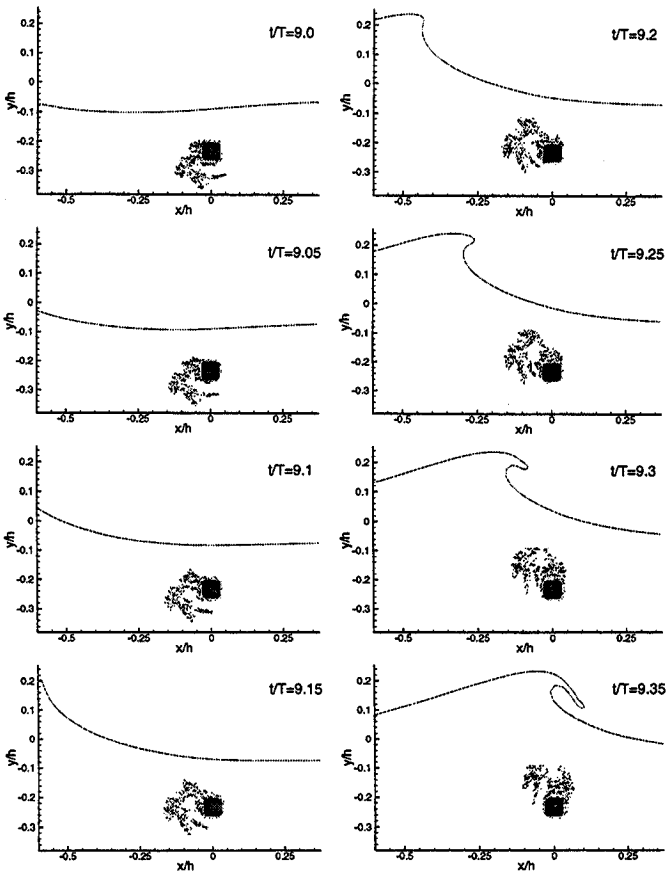

Figure 7: Evolution of the free surface and blobs prior to wave plunging.